J Nanopart Res (2015) 17:348
DOI 10.1007/s11051-015-3154-7

RESEARCH PAPER

Fe_3O_4 nanoparticles-wrapped carbon nanofibers as high-performance anode for lithium-ion battery

Fei Jiang · Saihua Zhao · Jinxin Guo · Qingmei Su · Jun Zhang · Gaohui Du

Received: 11 May 2015 / Accepted: 14 August 2015 / Published online: 25 August 2015
© Springer Science+Business Media Dordrecht 2015

Abstract One-dimensional hierarchical nanostructures composed of Fe_3O_4 nanoparticles and carbon nanofibers (CNFs) have been successfully synthesized through a facile solvothermal method followed by a simple thermal annealing treatment. X-ray diffraction and electron microscopy reveal that Fe_3O_4 nanoparticles with a size of 80–100 nm are uniformly dispersed on CNFs. The Fe_3O_4/CNFs nanocomposites show an enhanced reversible capacity and excellent rate performance as anode for Li-ion battery. The reversible capacity of the nanocomposites retains 684 mAh g^{-1} after 55 cycles at 100 mA g^{-1}. Even when cycled at various rate (100, 200, 500, 1000, and 2000 mA g^{-1}) for 50 cycles, the capacity can recover to 757 mAh g^{-1} at the current of 100 mA g^{-1}. The enhanced electrochemical performances are attributed to the characteristics of interconnected one-dimensional nanostructures that provide three-dimensional networks for Li-ion diffusion and electron transfer, and can further accommodate the volumetric change of Fe_3O_4 nanoparticles during charge–discharge cycling.

Keywords Nanostructures · Chemical synthesis · Electron microscopy · Energy storage

F. Jiang · S. Zhao · J. Guo · Q. Su · J. Zhang · G. Du (✉)
Institute of Physical Chemistry, Zhejiang Normal University, Jinhua 321004, China
e-mail: gaohuidu@zjnu.edu.cn

Introduction

In recent years, lithium-ion batteries (LIBs) with a high voltage, high specific capacity, environmental friendliness, and low cost have been paid great attention to use as the best power source for an extensive range of portable electronic devices, power tools, and electric vehicles (Bogart et al. 2014; Ma et al. 2014; Zhang et al. 2014). The performance of LIBs greatly depends on the properties of electrodes. Graphite is currently served as the standard anode material for LIBs. Nevertheless, the graphite anodes are handicapped due to their relatively low theoretical capacity (372 mAh g^{-1}) in LIBs (Zhang et al. 2012). Therefore, extensive efforts have been made to find alternative materials with higher capacities, including tin, silicon, and transitional metal oxide-based materials to replace graphite (Reddy et al. 2013; Qin et al. 2014; Yan et al. 2015; Xiao et al. 2014; Xie et al. 2013). However, these materials (e.g., Si, Sn, and metal oxides) show a large volume change during charge/discharge process and poor electrical conductivity, which lead to unsatisfactory cycling stability and rate performance, and seriously limit their applications.

Many approaches have been developed to solve the above problems. Anode materials with one-dimensional (1D) nanostructures have been extensively studied as they have great potential for enhancing electrical conductivity and relieving the volumetric

change during cycling (Guo et al. 2008; Jiang et al. 2011). Particularly, 1D carbon nanofibers (CNFs) have demonstrated their superiority as an effective carbon matrix to load active materials to achieve high electrochemical performance for LIB application due to their super electronic conductivity, undamaged morphology during cycling, and independent characteristic (Agend et al. 2007; Bonino et al. 2011). In addition, CNFs can accommodate the dramatic volumetric expansion of active materials during lithiation/delithiation, and thus improve the capacity retention of active materials by preventing the nanoparticle pulverization (Su et al. 2014) and the loss of electric contact between active substances and the current collector. On the other hand, iron oxide (Fe_3O_4)-based nanostructured materials are attracting great attention as high-performance anode materials for LIBs due to their high theoretical capacity (924 mAh g^{-1}), low toxicity, environmental friendliness, and the natural abundance of iron (Reddy et al. 2012; Wang et al. 2011; Wu et al. 2014; Lei et al. 2014; Liu et al. 2008; Choi et al. 2014). Recently, Fe_3O_4-based hybrid nanostructures, such as Fe_3O_4–graphene (Wang et al. 2011), Fe_3O_4–C composite (Wang et al. 2013), foam-like Fe_3O_4–carbon architectures (Wu et al. 2014), Fe_3O_4–carbon hollow particles (Lei et al. 2014), and Fe_3O_4–carbon core–shell nanorods (Liu et al. 2008) have been investigated as the potential architectures to improve the electrochemical performance in LIBs because the Fe_3O_4–carbon integrated materials could sustain their structural integrity during cycling (Xiong et al. 2012; Ma et al. 2012; Li et al. 2011).

In this work, we develop a simple solvothermal method followed by thermal annealing to fabricate 1D hierarchical Fe_3O_4/CNFs nanocomposites, which integrate the high-capacity Fe_3O_4 nanoparticles with highly conductive CNFs. Specifically, the CNFs serve as a supporting matrix for dispersing of Fe_3O_4 nanoparticles, resulting in large surface area and excellent electrical conductivity. The electrolyte can easily penetrate the porous CNFs network, leading to the increase of the contact area between electrolyte and active materials. Individual CNFs make direct contact with the current collectors, and provide a fast and efficient electron transfer pathway. As a result, the as-prepared Fe_3O_4/CNFs nanostructures show an improved electrochemical performance as anode for LIB application.

Experimental

Synthesis

The CNFs were synthesized through a modified hydrothermal method using Te nanowire as the template according to the previous literature (Liang et al. 2012). Fe_3O_4/CNFs nanocomposites were prepared by a simple solvothermal process with subsequent annealing treatment. First, 10 mg of CNFs and 15 ml of $FeCl_3$ (0.2 M) were dispersed in 120 ml of anhydrous ethanol by ultrasonic stirring. Then 4 ml of $NH_3{\cdot}H_2O$ was dropped into the above solution to produce uniform dispersion. The mixture was kept at 80 °C in a water bath with stirring for 24 h, and was subsequently transferred to a Teflon-lined autoclave and placed in an oven at 160 °C for 3 h. The resultant brown precursors were centrifuged, washed with distilled water and anhydrous ethanol, and were dried overnight at 60 °C. Finally, the precursors were calcined at 500 °C in Ar atmosphere for 3 h to obtain the Fe_3O_4/CNFs nanocomposites.

Characterization

The as-prepared samples were characterized using X-ray powder diffraction on a Philips PW3040/60 X-ray diffractometer with Cu Ka ($\lambda = 1.54056$ Å) radiation for phase identification. The content of CNFs in the Fe_3O_4/CNFs nanocomposites was ascertained by the thermogravimetric analysis measurement (TGA, Netzsch STA449C thermal analyzer). The morphologies were examined by scanning electron microscopy (SEM, Hitachi S-4800), and the microstructures were investigated by transmission electron microscopy (TEM, JEM 2010F).

Electrochemical test

The electrochemical performances of the Fe_3O_4/CNFs nanocomposites were investigated with two-electrode coin-type cells (CR2025). The working electrodes were prepared by dispersing the as-prepared Fe_3O_4/CNFs nanocomposites (75 wt%), and polyvinylidene fluorides (10 wt%) as binder, acetylene carbon black (15 wt%) as conducting additive in *N*-methyl-2-pyrrolidone solvent to form a slurry. The slurry was incorporated on nickel foam current collector and dried at 80 °C for 6 h in a vacuum oven. The loading

density of Fe_3O_4/CNFs nanocomposites was about 1.8–2 mg cm^{-2}. The test cells were assembled in an argon-filled glove box with the metallic lithium foil as both the counter and reference electrodes. The electrolyte solution was 1 M $LiPF_6$ dissolved in a mixture of ethylene carbonate and dimethyl carbonate with a volume ratio of 1:1. The cyclic voltammetry (CV) was carried out on a CHI660C electrochemistry workstation in the potential window of 0.02–3.0 V at a scan rate of 0.1 mV s^{-1}. The galvanostatic charge and discharge measurements were tested at a current density of 100 mA g^{-1} and the rate performance was conducted at different current densities (100, 200, 500, 1000, and 2000 mA g^{-1}) on a battery test system (Neware Co. Ltd., Shenzhen) in the voltage range from 0.005 to 3 V. The specific capacity was calculated based on the total mass of Fe_3O_4/CNFs nanocomposites in coin-type cells. AC impedance measurements were carried out using a CHI604D electrochemical workstation. The amplitude was 50 mV and the frequency ranged from 100 kHz to 10 mHz. The impedance data were fitted using the ZsimpWin computer program.

Results and discussion

The XRD pattern of the as-prepared Fe_3O_4/CNFs nanocomposites is shown in Fig. 1. All the diffraction peaks can be indexed to the face-centered cubic Fe_3O_4 with the lattice constant of $a = 8.394$ Å (JCPDS No. 89-3854). No other impurity phase is observed in the XRD pattern, and the sharp diffraction peaks reflect the excellent crystallinity of Fe_3O_4, confirming the high-purity phase of the products.

To estimate the amount of CNFs and Fe_3O_4 components in the nanocomposites, TGA was carried out in air with a heating rate of 10 °C/min from room temperature to 600 °C. TGA curve of the Fe_3O_4/CNFs nanocomposite was presented in Fig. 2. The slight weight loss between room temperature and 150 °C is about 1.0 %, corresponding to the evaporation of absorbed moisture in the sample, whereas the weight gain of about 1.3 % for Fe_3O_4/CNFs nanocomposites between 150 and 285 °C is likely the result of oxidation of the Fe_3O_4 in air (Zhu et al. 2011b). The sharp weight losses observed from 285 to 450 °C are mainly attributed to the oxidation and decomposition of CNFs. Calculated from the weight losses of CNFs and the mass gains of Fe_3O_4 due to oxidation, the amount of CNFs component in the nanocomposites is about 12.8 wt%.

The morphology and microstructure of Fe_3O_4/CNFs nanocomposites were investigated using SEM and TEM. Figure 3a shows a SEM image of the pristine CNFs with an average diameter of 300 nm; the lengths of CNFs range from several to tens of micrometers. The entangled CNFs interconnect with each other to a high degree through numerous junctions, which is advantageous for the electrochemical lithium storage performances due to the formation of 3D conductive network. Figure 3b, c shows SEM images of Fe_3O_4/CNFs nanocomposites. Fe_3O_4 nanoparticles are homogenously dispersed on the surface of CNFs. The fine dispersion and tight attachment of the Fe_3O_4 nanoparticles (80–100 nm) on individual CNFs is further revealed by TEM as shown in Fig. 3d, e. Figure 3f presents a HRTEM image of a Fe_3O_4 nanoparticle on CNFs (the inset is the fast Fourier transform pattern). The lattice fringes

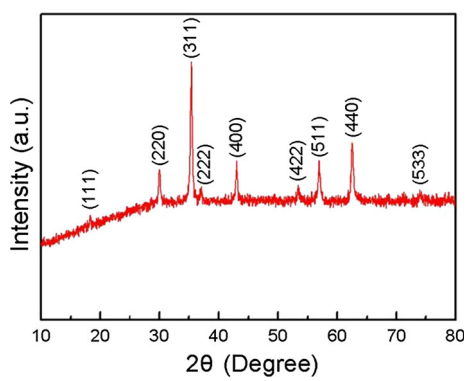

Fig. 1 XRD pattern of the Fe_3O_4/CNFs nanocomposites

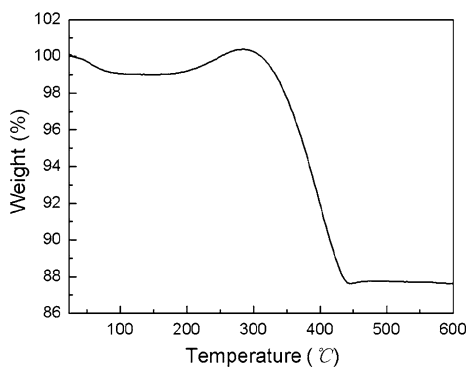

Fig. 2 TGA curve of the Fe_3O_4/CNFs nanocomposites

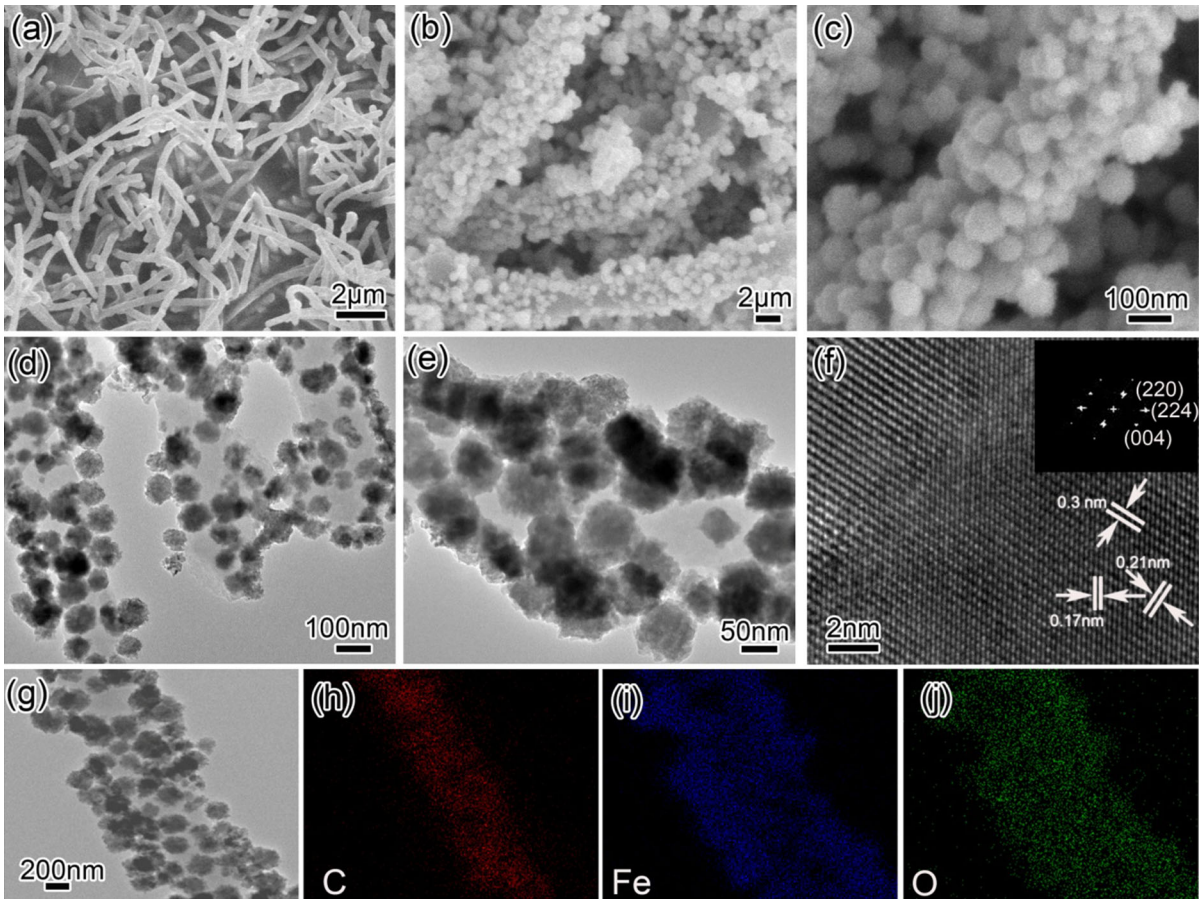

Fig. 3 **a** SEM image of the pristine CNFs. **b**, **c** SEM images of Fe_3O_4/CNFs nanocomposites. **d**, **e** TEM images of Fe_3O_4/CNFs nanocomposites. **f** HRTEM image of Fe_3O_4/CNFs nanocomposites and the corresponding FFT pattern (*inset*). **g**–**j** TEM image of Fe_3O_4/CNFs and corresponding mapping of carbon, iron, and oxygen elements

with spacing of 0.30, 0.21, and 0.17 nm can be assigned to (220), (004), and (224) planes of cubic Fe_3O_4, respectively, which is in agreement with the XRD result. Figure 3g, j shows a TEM image of Fe_3O_4/CNFs and the mapping of C, Fe, and O elements within this Fe_3O_4/CNFs nanocomposite, which further confirms the architecture of Fe_3O_4 nanoparticles dispersed on CNFs surface.

The electrochemical behavior and performance of the Fe_3O_4/CNFs nanocomposites were evaluated by CV and galvanostatic charge–discharge using two-electrode CR2025 coin-type cells. Figure 4a shows the CV curves of Fe_3O_4/CNFs nanocomposites electrode. A reduction peak at about 0.6 V is observed in the first cathodic scan for the Fe_3O_4/CNFs nanocomposites, which can be attributed to the reduction of Fe^{3+} and Fe^{2+} to Fe^0 and the formation of solid electrolyte interface (SEI) layer (Lei et al. 2014). Meanwhile, two anodic peaks at about 1.67 and 1.90 V correspond to the reversible oxidation of Fe^0 to Fe^{2+}/Fe^{3+}, which agrees well with early studies (Wu et al. 2014; Lian et al. 2010). During the subsequent cycles, both cathodic and anodic peaks are positively shifted, which is attributed to the structural change of the electrode materials induced by the first lithiation process due to the irreversibility. The CV curves are found to be coincided after the first cycle, which indicates the good electrochemical reversibility and stability of Fe_3O_4/CNFs nanocomposites.

Figure 4b shows the galvanostatic discharge–charge curves of the Fe_3O_4/CNFs nanocomposite electrodes between 0.005 and 3 V at a current density

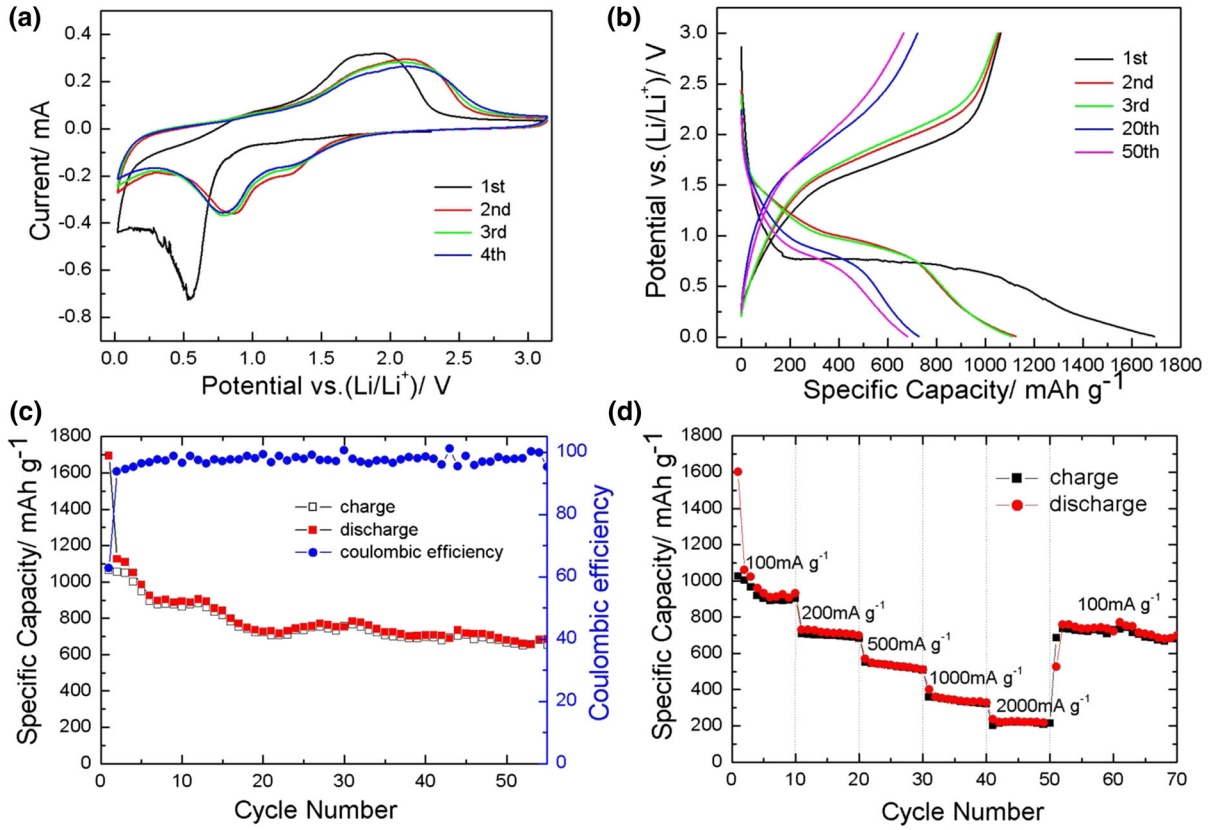

Fig. 4 Electrochemical measurement of Fe_3O_4/CNFs nanocomposite electrodes. **a** CV curves at a scan rate of 0.1 mV s^{-1}. **b** Voltage profiles for the selected galvanostatic cycles at a current density of 100 mA g^{-1}. **c** Reversible charge/discharge capacities against cycle number at a current density of 100 mA g^{-1}. **d** Rate performance of the electrode at the current of 100, 200, 500, 1000, 2000, and 100 mA g^{-1}

of 100 mA g^{-1}. In the first discharge step, a long voltage plateau can be observed at about 0.75 V, followed by a sloping curve down to the cut voltage of 5 mV, which are the typical characteristics of voltage profile for Fe_3O_4 (Wu et al. 2014; He et al. 2010). From the second cycle, this discharge plateau becomes much shorter and shifts to higher voltage, indicating the different lithiation behaviors between the first and the subsequent cycles; there are irreversible reactions during the first cycle, such as the formation of SEI layer and irreversible phase conversion (Su et al. 2013). Meanwhile, the main plateau from 1.6 to 1.9 V during charging can be attributed to the oxidation of Fe^0 to Fe^{2+} and Fe^{3+} (He et al. 2010; Xia et al. 2013). These results agree well with the CV analysis.

Figure 4c shows the cycling performance of Fe_3O_4/CNFs electrodes at the constant current density of 100 mA g^{-1}. The initial discharge and charge capacity of Fe_3O_4/CNFs nanocomposites is 1694 and 1063 mAh g^{-1}, which is larger than the theoretical capacity of Fe_3O_4 (926 mAh g^{-1}). The extra capacity of the electrodes compared with the theoretic capacity results from the formation of solid electrolyte interface SEI film and possibly interfacial Li^+ ion storage during the discharge process (Chou et al. 2010; Débart et al. 2001). The Coulomb efficiency in the first cycle is about 63 %. The initial capacity loss of 37 % mainly results from the diverse irreversible process, like electrolyte decomposition and inevitable formation of SEI layer, and irreversible phase conversion (Su et al. 2013), which are similar to most metal oxide anode materials (Xu et al. 2012; Wu et al. 2012; Zhu et al. 2011a; Zhang et al. 2008). The Coulomb efficiency reaches 93 % in the second cycle and remains relatively stable at 97 % in the subsequent cycles. The reversible discharge capacity of Fe_3O_4/CNFs

electrode remains 684 mAh g^{-1} after 55 cycles at 100 mA g^{-1}.

The rate performance of Fe_3O_4/CNFs nanocomposite has been evaluated. As we can see in Fig. 4d, the specific capacity of the Fe_3O_4/CNFs nanocomposites is 930, 700, 511, 326, and 211 mAh g^{-1} after each ten cycles for the current density of 100, 200, 500, 1000, and 2000 mA g^{-1}, respectively. When the current density is reduced back to 100 mA g^{-1}, the Fe_3O_4/CNFs electrode can recover a capacity of 757 mAh g^{-1}. The results indicate that the Fe_3O_4/CNFs nanocomposites can tolerate high current cycling and have good retention of capacity. Although the performance of Fe_3O_4/CNFs nanocomposites is not as good as the Fe_3O_4–CNT (Wu et al. 2013), hierarchical Fe_3O_4 microsphere/graphene nanosheet composite (Wang et al. 2014), and 600 °C carbonized C/Fe_3O_4 nanofibers (Wang et al. 2008), but superior to Fe_3O_4/carbon core–shell nanorods (Li et al. 2011), Fe_3O_4 nanocubes (Cao et al. 2011), Fe_3O_4/Fe/carbon composite (Zhao et al. 2012), 500 °C carbonized C/Fe_3O_4 nanofibers (Wang et al. 2008), and Fe_3O_4 nanotube (Xia et al. 2013). The excellent electrochemical behaviors can be attributed to several aspects: (1) The CNFs after annealing in Ar at high temperature have enhanced conductivity. (2) The interconnected 1D Fe_3O_4/CNFs nanocomposites can provide 3D continuous conducting pathways for Li^+ and e^- transports within the electrode. (3) During the charge/discharge process, the space among CNFs can accommodate the serious volume change of Fe_3O_4 nanoparticles and thus enhance the structural stability of electrodes.

Electrochemical impedance spectroscopy (EIS) of Fe_3O_4/CNFs nanocomposites was investigated to understand the kinetics that influences the electrochemical reaction toward lithium. The EIS measurements were performed before the first cycling and after the 55th cycling test. As shown in Fig. 5a, the Nyquist plots consist of a semicircle in the high- and middle-frequency regions, and a straight line in the low-frequency region. The classic equivalent circuit as shown in Fig. 5b is adopted to model the electrochemical system, where R_e represents the resistance of the electrolyte, and R_{sl} and C_{sl} are designated for the resistance of the migration and capacity of the layer in the high-frequency semicircle. R_{ct} and C_{dl} are associated with the charge transfer resistance and a double-layer capacitance in the medium-frequency

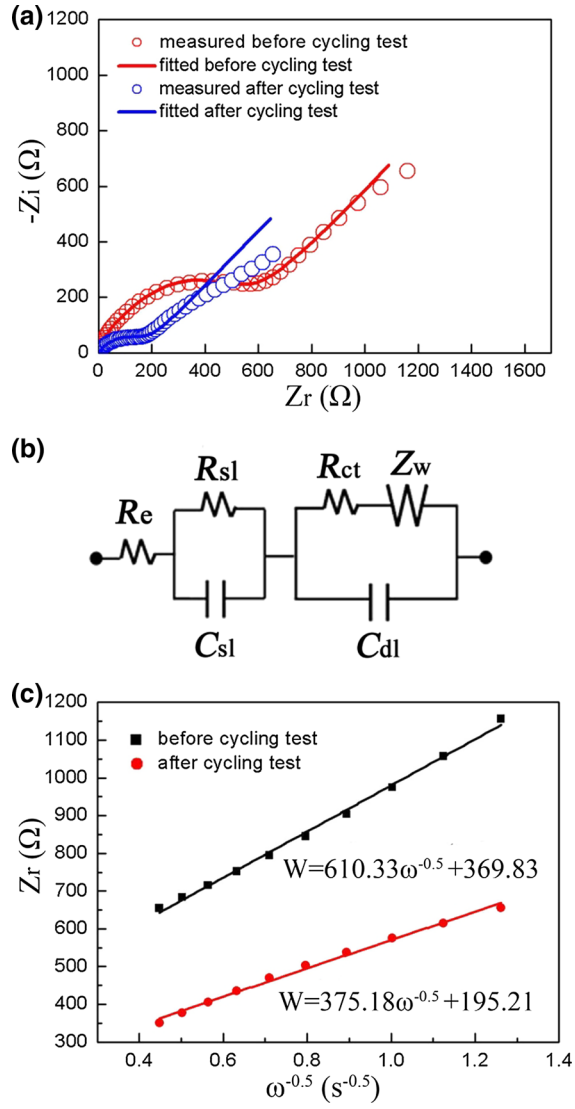

Fig. 5 **a** Nyquist plots of the Fe_3O_4/CNFs electrode obtained by applying a sine wave with amplitude of 5.0 mV over the frequency range from 100 kHz to 0.01 Hz. **b** Equivalent circuit for Fe_3O_4/CNFs electrode/electrolyte interface. **c** Relationship between Z_r and $\omega^{-0.5}$ in the frequency region of 0.1–0.01 Hz

semicircle, and Z_W represents the diffusion-controlled Warburg impedance. The main parameters calculated according to the equivalent circuit are presented in Table 1. The charge transfer resistance (R_{ct}, 0.439 Ω) after the 55th cycles is significantly smaller than the R_{ct} (291 Ω) before cycling. The reduced R_{ct} indicates more sufficient contact between active materials and electrolyte with cycling (Wu et al. 2014). The relationship between real impedance Z_r and the reciprocal root square of the lower angular

Table 1 Electrochemical impedance parameters of Fe_3O_4/CNFs nanocomposites before cycling and after the 55th cycle

Sample	R_e (Ω)	R_{ct} (Ω)	σ (Ω $s^{-0.5}$)	D (cm^2 s^{-1})	i^o (Ma cm^{-2})
Before cycling	2.572	291	610.33	3.96×10^{-13}	1.10×10^{-5}
After cycling	0.591	0.439	375.18	1.05×10^{-12}	7.31×10^{-3}

frequency $\omega^{-0.5}$ for the nanocomposites before the first cycling and after the 55th cycling test is displayed in Fig. 5c. Linear behaviors with different slopes are observed in the two curves. We can achieve the Warburg factor σ and calculate the diffusion coefficient D and the exchange current density i^o according to Eqs. (1) and (2) (Shenouda and Liu 2010; Xiang et al. 2011a), and the values are listed in Table 1.

$$D = 0.5(RT/AF^2\sigma C)^2 \quad (1)$$

$$i^o = RT/nFR_{ct} \quad (2)$$

where n is the number of electrons per molecule during reaction; A is the active surface area of the electrode; R is the gas constant; T is the absolute temperature; F is the Faraday constant; and C is the molar concentration of Li^+ ions. From Fig. 5c, we can see that the Warburg impedance coefficient (σ) is 375.18 Ω $s^{-0.5}$ after 55 cycles, and it has a lower value than that (610.33 Ω $s^{-0.5}$) before cycling. The obtained diffusion coefficient ($D = 1.05 \times 10^{-12}$ cm^2 s^{-1}) after cycling explains the higher mobility of Li^+ ions than that before cycling ($D = 3.96 \times 10^{-13}$ cm^2 s^{-1}). Moreover, the exchange current density (i^o) is 7.31×10^{-3} mA cm^{-2} after cycling, which is higher than 1.10×10^{-5} mA cm^{-2} before cycling. It is generally believed that the process of charge transfer occurs mainly on the active materials/electrolyte interfaces, so the surface morphology and microstructure of the electrode materials are the most important factors affecting the electrochemical impedance during the discharge/charge process (Xiang et al. 2011b). The conversion reaction occurred during the first lithiation/delithiation process and the electrode volume expansion/shrinkage make Fe_3O_4 particles convert to ultrafine nanograins (Su et al. 2013), which can increase the surface area of the active materials, shorten Li^+ diffusion route, and facilitate charge transfer on active materials/electrolyte interfaces. In other words, the structural modification in the Fe_3O_4/CNFs electrode owing to the lithiation/delithiation processes leads to the decrease of charge transfer resistance and significant enhancement of the diffusion coefficient and exchange current density. So the charge transfer reaction after cycling is much stronger than that before cycling. The higher diffusion coefficient and exchange current density and lower charge transfer resistance after the 55th cycle account for the stable cycling and excellent rate performances of the Fe_3O_4/CNFs nanocomposites.

Conclusion

In summary, we have successfully synthesized Fe_3O_4/CNFs nanocomposites by a facile two-step method involving the solvothermal synthesis and subsequent thermal annealing. The CNFs are found to be attached by many uniform Fe_3O_4 nanoparticles around 80–100 nm. The as-prepared Fe_3O_4/CNFs nanocomposites demonstrate extraordinary electrochemical performance, such as high capacity, long cycling stability (684 mAh g^{-1} after 55 cycles at 100 mA g^{-1}), and excellent rate capability. The greatly improved electrochemical performance can be attributed to the interconnected 1D nanostructures that provide efficient pathways for Li-ion diffusion and electron transfer, and can also accommodate the volumetric change of Fe_3O_4 nanoparticles during cycling. Our results reveal a new approach to Fe_3O_4/CNFs nanocomposites with great potential as anode material in LIBs.

Acknowledgments This work was supported by the Program for New Century Excellent Talents in University of Ministry of Education of China (NCET-11-1081) and the National Science Foundation of China (No. 21203168).

References

Agend F, Naderi N, Fareghi-Alamdari R (2007) Fabrication and electrical characterization of electrospun polyacrylonitrile-derived carbon nanofibers. J Appl Polym Sci 106:255–259

Bogart TD, Oka D, Lu XT, Gu M, Wang CM, Korgel BA (2014) Lithium ion battery performance of silicon nanowires with carbon skin. ACS Nano 8:915–922

Bonino CA, Ji L, Lin Z, Toprakci O, Zhang X, Khan SA (2011) Electrospun carbon-tin oxide composite nanofibers for use as lithium ion battery anodes. ACS Appl Mater Interfaces 3:2534–2542

Cao H, Liang R, Qian D, Shao J, Qu M (2011) L-serine-assisted synthesis of superparamagnetic Fe_3O_4 nanocubes for lithium ion batteries. J Phys Chem C 115:24688–24695

Choi SH, Ko YN, Jung KY, Kang YC (2014) Macroporous Fe_3O_4/carbon composite microspheres with a short Li^+ diffusion pathway for the fast charge/discharge of lithium ion batteries. Chem Eur J 20:11078–11083

Chou SL, Wang JZ, Wexler D, Konstantinov K, Zhong C, Liu HK, Dou SX (2010) High-surface-area α-Fe_2O_3/carbon nanocomposite:one-step synthesis and its highly reversible and enhanced high-rate lithium storage properties. J Mater Chem 20:2092–2098

Débart A, Dupont L, Poizot P, Leriche JB, Tarascon JM (2001) A transmission electron microscopy study of the reactivity mechanism of tailor-made CuO particles toward Lithium. J Electrochem Soc 148:A1266–A1274

Guo YG, Hu JS, Wan LJ (2008) Nanostructured materials for electrochemical energy conversion and storage devices. Adv Mater 20:2878–2887

He Y, Huang L, Cai JS, Zheng XM, Sun SG (2010) Structure and electrochemical performance of nanostructured Fe_3O_4/carbon nanotube composites as anodes for lithium ion batteries. Electrochim Acta 55:1140–1144

Jiang J, Li Y, Liu J, Huang X (2011) Building one-dimensional oxide nanostructure arrays on conductive metal substrates for lithium-ion battery anodes. Nanoscale 3:45–58

Lei C, Han F, Sun Q, Li WC, Lu AH (2014) Confined nanospace pyrolysis for the fabrication of coaxial Fe_3O_4@ C hollow particles with a penetrated mesochannel as a superior anode for Li-ion batteries. Chem Eur J 20:139–145

Li B, Cao H, Shao J, Qu M (2011) Enhanced anode performances of the Fe_3O_4–carbon–rGO three dimensional composite in lithium ion batteries. Chem Commun 47:10374–10376

Lian P, Zhu X, Xiang H, Li Z, Yang W, Wang H (2010) Enhanced cycling performance of Fe_3O_4–graphene nanocomposite as an anode material for lithium-ion batteries. Electrochim Acta 56:834–840

Liang HW, Guan QF, Chen LF, Zhu Z, Zhang WJ, Yu SH (2012) Macroscopic-scale template synthesis of robust carbonaceous nanofiber hydrogels and aerogels and their applications. Angew Chem Int Ed 51:5101–5105

Liu H, Wang G, Wang J, Wexler D (2008) Magnetite/carbon core-shell nanorods as anode materials for lithium-ion batteries. Electrochem Commun 10:1879–1882

Ma Y, Zhang C, Ji G, Lee JY (2012) Nitrogen-doped carbon-encapsulation of Fe_3O_4 for increased reversibility in Li^+ storage by the conversion reaction. J Mater Chem 22:7845–7850

Ma YC, Huang YD, Wang XC, Jia DZ, Tang XC (2014) One-pot synthesis of Fe_3O_4/C nanocomposites by PEG-assisted co-precipitation as anode materials for high-rate lithium-ion batteries. J Nanopart Res 16:2614

Qin J, He CN, Zhao NQ, Wang ZY, Shi CS, Liu EZ, Li JJ (2014) Graphene networks anchored with Sn@ graphene as lithium ion battery anode. ACS Nano 8:1728–1738

Reddy ALM, Gowda SR, Shaijumon MM, Ajayan PM (2012) Hybrid nanostructures for energy storage applications. Adv Mater 24:5045–5064

Reddy MV, Subba Rao GV, Chowdari BV (2013) Metal oxides and oxysalts as anode materials for Li ion batteries. Chem Rev 113:5364–5457

Shenouda AY, Liu HK (2010) Preparation, characterization, and electrochemical performance of Li_2CuSnO_4 and $Li_2CuSnSiO_6$ electrodes for lithium batteries. J Electrochem Soc 157:A1183–A1187

Su QM, Xie D, Zhang J, Du GH, Xu BS (2013) In situ transmission electron microscopy observation of the conversion mechanism of Fe_2O_3/graphene anode during lithiation–delithiation processes. ACS Nano 7:9115–9121

Su QM, Xie J, Zhang J, Zhong YJ, Du GH, Xu BS (2014) In situ transmission electron microscopy observation of electrochemical behavior of CoS_2 in lithium-ion battery. ACS Appl Mater Interfaces 6:3016–3022

Wang L, Yu Y, Chen PC, Zhang DW, Chen CH (2008) Electrospinning synthesis of C/Fe_3O_4 composite nanofibers and their application for high performance lithium-ion batteries. J Power Sources 183:717–723

Wang JZ, Zhong C, Wexler D, Idris NH, Wang ZX, Chen LQ, Liu HK (2011) Graphene-encapsulated Fe_3O_4 nanoparticles with 3D laminated structure as superior anode in lithium ion batteries. Chem Eur J 17:661–667

Wang P, Gao MX, Pan HG, Zhang JL, Liang C, Wang JH, Zhou P, Liu YF (2013) A facile synthesis of Fe_3O_4/C composite with high cycle stability as anode material for lithium-ion batteries. J Power Sources 239:466–474

Wang TQ, Wang XL, Lu Y, Xiong QQ, Zhao XY, Cai JB, Huang S, Gu CD, Tu JP (2014) Self-assembly of hierarchical Fe_3O_4 microsphere/graphene nanosheet composite:towards a promising high-performance anode for Li-ion batteries. RSC Adv 4:322–430

Wu H, Xu M, Wu HY, Xu JJ, Wang YL, Peng Z, Zheng GF (2012) Aligned NiO nanoflake arrays grown on copper as high capacity lithium-ion battery anodes. J Mater Chem 22:19821–19825

Wu Y, Wei Y, Wang J, Jiang K, Fan S (2013) Conformal Fe_3O_4 sheath on aligned carbon nanotube scaffolds as high-performance anodes for lithium ion batteries. Nano Lett 13:818–823

Wu F, Huang R, Mu D, Wu B, Chen S (2014) New synthesis of a foamlike Fe_3O_4/C composite via a self-expanding process and its electrochemical performance as anode material for lithium-ion batteries. ACS Appl Mater Interfaces 6:19254–19264

Xia H, Wan Y, Yuan G, Fu Y, Wang X (2013) Fe_3O_4/carbon core–shell nanotubes as promising anode materials for lithium-ion batteries. J Power Sources 241:486–493

Xiang JY, Tu JP, Qiao YQ, Wang XL, Zhong J, Zhang D, Gu CD (2011a) Electrochemical impedance analysis of a hierarchical CuO electrode composed of self-assembled nanoplates. J Phys Chem C 115:2505–2513

Xiang JY, Wang XL, Zhong J, Zhang D, Tu JP (2011b) Enhanced rate capability of multi-layered ordered porous

nickel phosphide film as anode for lithium ion batteries. J Power Sources 196:379–385

Xiao AG, Zhou SB, Zuo CG, Zhuan YB, Ding X (2014) Controllable synthesis of mesoporous Co_3O_4 nanoflake array and its application for supercapacitor. Mater Res Bull 60:674–678

Xie D, Yuan WW, Dong ZM, Su QM, Zhang J, Du GH (2013) Facile synthesis of porous NiO hollow microspheres and its electrochemical lithium-storage performance. Electrochim Acta 92:87–92

Xiong QQ, Tu JP, Lu Y, Chen J, Yu YX, Qiao YQ, Wang XL, Gu CD (2012) Synthesis of hierarchical hollow-structured single-crystalline magnetite (Fe_3O_4) microspheres: the highly powerful storage versus lithium as an anode for lithium ion batteries. J Phys Chem C 116:6495–6502

Xu X, Cao R, Jeong S, Cho J (2012) Spindle-like mesoporous α-Fe_2O_3 anode material prepared from mof template for high-rate lithium batteries. Nano Lett 12:4988–4991

Yan JF, Wang G, Wang H, Zhang ZY, Ruan XF, Zhao W, Yun JN, Xu MZ (2015) Preparation and electrochemical performance of bramble-like ZnO array as anode materials for lithium-ion batteries. J Nanopart Res 17:52

Zhang WM, Wu XL, Hu JS, Guo YG, Wan LJ (2008) Carbon coated Fe_3O_4 nanospindles as a superior anode material for lithium-ion batteries. Adv Funct Mater 18:3941–3946

Zhang C, Wang Z, Guo Z, Lou XW (2012) Synthesis of MoS_2-C one-dimensional nanostructures with improved lithium storage properties. ACS Appl Mater Interfaces 4:3765–3768

Zhang J, Xiang JY, Dong ZM, Liu Y, Wu YS, Xu CM, Du GH (2014) Biomass derived activated carbon with 3D connected architecture for rechargeable lithium-sulfur batteries. Electrochim Acta 116:146–151

Zhao X, Xia D, Zheng K (2012) Fe_3O_4/Fe/carbon composite and its application as anode material for lithium-ion batteries. ACS Appl Mater Interfaces 4:1350–1356

Zhu J, Sharma YK, Zeng Z, Zhang X, Srinivasan M, Mhaisalkar S, Zhang H, Hng HH, Yan Q (2011a) Cobalt oxide nanowall arrays on reduced graphene oxide sheets with controlled phase, grain size, and porosity for li-ion battery electrodes. J Phys Chem C 115:8400–8406

Zhu T, Chen JS, Lou XW (2011b) Glucose-assisted one-pot synthesis of FeOOH nanorods and their transformation to Fe_3O_4@ carbon nanorods for application in lithium ion batteries. J Phys Chem C 115:9814–9820